行政院國家科學委員會專題研究計畫成果報告

微型熱管內流動現象的理論分析

計畫類別：☑個別型計畫　　　□整合型計畫
計畫編號：NSC90-2212-E-002-191
執行期間：90年8月1日至91年7月31日

計畫主持人：賴君亮

本成果報告包括以下應繳交之附件：
- □赴國外出差或研習心得報告一份
- □赴大陸地區出差或研習心得報告一份
- □出席國際學術會議心得報告及發表之論文各一份
- □國際合作研究計畫國外研究報告書一份

執行單位：國立台灣大學機械工程學系

中華民國九十一年七月三十一日

茲爲編造九十一學年度碩、博士班研究生導生名冊，敬請惠就尊任指導各年級碩、博士班研究生（含碩、博士班本學年度入學新生）姓名核對於下表，並請於 10 月 4 日前擲交系辦李芳菁爲感。此致

各教授

※碩、博士班各年級研究生學號、姓名放置系辦隔壁教師休息室沙發前長型小方桌上，以供參考。

碩士班研究生			博士班研究生		
年級	學號	姓名	年級	學號	姓名
指導教授（請簽名）：					

d:\李芳菁\雜項\導生名冊表格

誌 謝

本研究計畫在中華民國國家科學委員會的贊助下得以順利完成, 特此深致謝意。

中文摘要

楔形渠道內液體的流動與傳輸現象是微型熱管藉以達成散熱功能的主要方式之一。大部分的理論研究都僅限於微型熱管在穩態操作條件下的分析與探討，或者忽略蒸氣與液面摩擦阻力及渠道內液體截面積變化的效應。鑑於此，本研究計畫乃針對楔形渠道內的暫態流動現象進行理論分析，並探討液面摩擦阻力，楔形角(wedge angle)與液面接觸角(contact angle)(後二因素將決定楔形渠道內流體的截面積)的影響效應。

本文將首先探討當自由液面受到一均勻剪應力的作用時楔形渠道內的暫態流動現象，並針對此剪應力以及楔形角與接觸角的變化對液柱(liquid column)截面上的流速分佈以及液柱移動速度的影響進行有系統的分析與探討。當假設重力加速度、慣性效應、延流動方向的液面曲率變化可忽略，以及液面受到一均勻的剪應力作用時，則 Weislogel and Lichter [19] 的相似解依然適用。計算結果顯示當剪應力作用與液柱的移動同向時，楔形渠道內的流動將加強，液柱的移動速度也將加快。而當剪應力作用與液柱的流動反向時，在液面靠近楔形渠道壁面的角落處將首先產生反向流動；當反向剪應力逐漸加強時，此反向流動區域將逐漸向渠道中央擴展。隨著時間的推展，液柱的移動將趨緩，並從所謂的等流量流域(constant-flow-rate regime) 過渡到等高度流域(constant-height regime)。而當液面受到一非均勻的剪應力作用時，相似解將不復存在，而有賴於數值計算來進行理論分析。

Abstract

The capillary flow and transport phenomenon in wedges are applied in micro heat pipes to achieve the removal of heat in many applications. Most of the theoretical works in the past dealt with the steady-state phenomena or neglected the effects due to the variation of the cross-sectional area of the wedge flow and the shear-stress distribution on the free surface between the liquid and vapor phases. The present research is therefore aimed at resolving these deficiencies to investigate theoretically the transient capillary flow phenomena in a wedge. The effects due to the shear stress imposed on the free surface, the contact angles, and the wedge angle (the later two factors determine the cross-sectional area of the wedge flow) are systematically analyzed and discussed.

The transient capillary wedge flow with a constant shear stress distribution imposed on the free surface is investigated. Effects on the velocity distribution and tip location of the wedge flow due to the variation of the half-wedge angle, contact angle, and the shear stress distribution on the free surface are systematically studied and discussed. With the assumptions of micro-gravity, small inertia, a slender liquid column with negligible surface curvature along the flow direction, and a constant shear stress distribution on the free surface, the similarity solutions as suggested by Weislogel and Lichter 〔19〕 are still valid. The results indicate that when the shear stress distribution acts in the flow direction, the wedge flow is strengthened with a larger propagation speed of the tip while when the shear stresses are opposing the flow direction, a reverse flow may start to occur in the corner region near the free surface. The reverse flow region extends toward the central portion of the cross section of the wedge flow when the countercurrent shear stresses become stronger. As time proceeds, the wedge flow slows down and moves from the constant-flow-rate regime toward the constant-height regime. If the shear stress distribution varies along the flow direction, similarity solutions may not exist and numerical computations have to be employed.

Contents

List of Tables

List of Figures

I. Introduction

The capillary pumping flows arise in various industrial applications and are of technical interests. On earth, these flows are usually negligible or limited in extent due to the presence of gravity, as can be seen from the Bond number, $Bo \equiv \Delta\rho \cdot g \cdot L^2 / \sigma$, with $\Delta\rho$ denoting the density difference across the fluid interface; g, the gravity; L, the characteristic length scale, and σ, the surface tension. However, the capillary pumping flows still have various terrestrial applications, such as flows in porous media and flows spreading along interior corners or grooves as faced in the oil industry, environmental technology, etc. In the micro-gravity environment of space, such flows and the capillary effect may become prevalent in fluid systems of large extent and possess particular importance in space technology. In-space applications include all kinds of fluid management and control such as the handling and storage of fuels propellants and biological wastes, design of heat exchangers and heat pipes, etc.

Investigations on the capillary pumping flows in interior corners, which also called grooves or wedges, in the past four decades have covered problems of static interfacial shape, dynamic flow behavior, and instability phenomenon. The effects of contact angle (θ) and wedge angle (2α) on the capillary statics were well addressed in the literature. The spreading of the capillary pumping flow along the wedge depends also on the contact angle and wedge angle. The criterion, $\theta < \frac{\pi}{2} - \alpha$, for a spontaneous wicking into the wedges were derived by Concus and Finn, which has been referred to as the Concus-Finn condition. Since then, a great number of investigation have been devoted to the flow behavior and heat transfer in grooves, both theoretically and experimentally. Instability and breakup of annular flows also attracted a significant amount of attention with technical importance in applications.

Most of the studies on the dynamics centered on the steady-state flow behavior and heat transfer. Weislogel and Lichter presented an asymptotic formulation on the limit of a slender fluid column with small inertia and solved analytically the tip location of a transient capillary flow in an interior corner. In their analysis, the zero shear stress conditions on the free surface were assumed and similarity solutions for the flow resistance, F_i, were then obtained. However, in many applications, especially in heat pipe, the interaction between the wedge flow and the gaseous (or vapor) flow on the free surface are important. In order to investigate the interaction effects on the velocity distribution of the wedge flow and the motion of the tip location, the analysis by Weislogel and Lichter is extended in the present study to incorporate a constant-shear-stress boundary condition on the free surface.

II. Assumptions and Formulation

The system to be analyzed is a capillary pumping flow along an interior corner of a container, a wedge, or a groove with a constant shear stress distribution imposed on the free surface. The schematic diagram of the physical model and the coordinate system employed are shown in Fig.1. In order to simplify the mathematical manipulation, the following assumptions are made:

(1) The lubrication approximation is applied to the wedge flow.

(2) A slender fluid column with negligible surface curvature along the flow direction is assumed.

(3) A circular arc of the interface is assumed for each cross section of the wedge flow.

(4) A static contact angle is employed. This approximation is acceptable when the fluid velocity perpendicular to the contact line is small.

(5) The gravity is negligibly small.

With the above assumptions, the leading-order momentum equations reduced to the cross-flow problem with the Z-component velocity as the main variable driven by the pressure gradient along the flow direction. The pressure distribution, to the leading order, is a function of Z and t only, i.e., $P = P(Z,t)$, which indicates a circular arc interface at each cross section, as stated in assumption (3).

In order to solve the variation of the interface as the liquid flows downstream the wedge and to find the tip location of the wedge flow and its propagation with time, the continuity equation in the following dimensionless form has to be solved with the momentum equation

$$A_t = -\dot{Q}_Z = -(A\overline{w})_Z \quad , \tag{1}$$

where A, $\dot{Q}$, and $\overline{w}$ are, respectively, the dimensionless cross-sectional area of the wedge flow, the volume flow rate, and the averaged Z-component velocity, i.e., $\overline{w} = \dot{Q}/A$ at each cross section.

By introducing the flow coefficient, F_i, as defined by Weislogel and Lichter (Weislogel and Lichter named F_i the flow resistance. However, since $F_i \propto \overline{w}$, it is proper to call F_i the flow coefficient and its inverse the flow resistance.) the dimensionless averaged Z-component velocity, $\overline{w}$, at each cross section can be expresses as follows

$$\overline{w} = -F_i h^2 P_Z = -F_i h_Z \quad , \tag{2}$$

where $P = -1/h$, as can be derived from the geometric configuration of the cross section, has been used. Equation (2) indicates that the averaged velocity $\overline{w}$

(nondimensionalized by $\left(\sigma \cdot H_o \cdot \sin^2 \alpha \middle/ \mu \cdot L_o\right)$ as suggested by Weislogel and Lichter) is determined solely by the slope of the interface, h_Z. As a result, there may exist a finite propagation speed even at the tip of the liquid column where $h = 0$ but h_Z possesses a finite value.

Substituting the above expression for $\overline{w}$ into Eq. (1) and noting that $A \propto h^2$ yields

$$2h_t = F_i\left(2h_Z^2 + h \cdot h_{ZZ}\right) . \qquad (3)$$

Since F_i is a function of α, θ, and the shear stress distribution along the free surface, it will be a constant for fixed values of α , θ , and the shear stress distribution. As suggested by Weislogel and Lichter, defining

$$h = \tau^a F(\eta) \ , \ \eta = |b|^{1/2} Z \tau^b \ , \ l_{tip} = \eta_{tip} |b|^{-1/2} \tau^{-b} \ ,$$

with $\tau = F_i t/2$ and $b = -(1+a)/2$, leads Eq. (3) to a similarity equation. In order to adding one more degree of freedom to the similarity variable, they further introduce the following transformation

$$F = \lambda^2 \widetilde{F} \quad , \quad \eta = \lambda \widetilde{\eta} \ . \qquad (4,5)$$

The tip location can then be assigned as $\widetilde{\eta}_{tip} = 1$ for the convenience of computation. With the above transformations, Eq. (3) is finally reduced to the following similarity equation

$$\widetilde{F} \cdot \widetilde{F}_{\widetilde{\eta}\widetilde{\eta}} + 2\widetilde{F}_{\widetilde{\eta}}^2 + \widetilde{\eta} \cdot \widetilde{F}_{\widetilde{\eta}} - \frac{2a}{1+a}\widetilde{F} = 0 \ , \qquad (6)$$

subject to $h(l_{tip}, \tau) = F(\eta_{tip}) = \widetilde{F}(\widetilde{\eta}_{tip}) = \widetilde{F}(1) = 0$, and $\widetilde{F}_{\widetilde{\eta}}(\widetilde{\eta}_{tip}) = \widetilde{F}_{\widetilde{\eta}}(1) = -\widetilde{\eta}_{tip}/2 = -1/2$.

Before solving Eq. (6), F_i must be evaluated first to render the validity of the similarity equation and solutions. However, since

$$F_i = \frac{\overline{w} \cdot (r_c/H)^2}{\sin^2 \alpha} = \frac{\overline{w}}{\sin^2 \alpha}\left(\frac{\cos\theta}{\sin\alpha} - 1\right)^{-2} \ , \qquad (7)$$

$\overline{w}$ must be computed before F_i can be evaluated. In Eq. (7), the following relation has been used

$$\frac{r_c}{H}=\left(\frac{\cos\theta}{\sin\alpha}-1\right)^{-1}\quad, \tag{8}$$

which can be derived from Fig. (1c), the geometric configuration of any cross section of the wedge flow. Therefore, the numerical computations of the w-distribution and the corresponding averaged velocity, $\overline{w}$, at any cross section will be presented in next section.

III. Numerical Computations

For the convenience of numerical computations, the cylindrical coordinates system located at the center of the circular arc of the interface and the following nondimensionalization scheme will be temporarily used. Relevant variables have to be converted to those defined by Weislogel and Lichter [19] for the convenience of comparison and justification of the validity of the present results. With the assumptions stated in last section and the following nondimensionalization scheme

$$v_Z = \frac{W}{\left[r_c^2 \left(-\frac{dP}{dZ} \right) \Big/ \mu \right]} \quad , \quad \xi = \frac{r}{r_c} \quad , \tag{9,10}$$

the Z-component momentum equation at any cross section of the wedge flow can be written as

$$\frac{\partial^2 v_Z}{\partial \xi^2} + \frac{1}{\xi}\frac{\partial v_Z}{\partial \xi} + \frac{1}{\xi^2}\frac{\partial^2 v_Z}{\partial \delta^2} + 1 = 0 \quad . \tag{11}$$

The associated boundary conditions are as follows

$$\frac{\partial v_Z}{\partial \xi} = S \quad , \text{on } \xi = \frac{r_c}{r_c} = 1 \quad , \tag{12}$$

$$v_Z = 0 \quad , \text{on } \xi = \frac{r_w}{r_z} = \frac{\cos\theta}{\sin(\alpha + \delta)} \quad , \tag{13}$$

$$\frac{\partial v_Z}{\partial \delta} = 0 \quad , \text{on } \delta = 0 \, . \tag{14}$$

Equation (12) indicates a dimensionless shear stress distribution in the Z-direction along the free surface while Eq. (13) and Eq. (14) represent, respectively, boundary conditions at the solid walls and the symmetrical condition at the mid-plane of the wedge.

In order to attain better accuracy of the numerical results with a more uniform distribution of the computational grids, the following nonequally spaced grid points in δ-direction is employed

$$\delta_j = \delta_o \frac{\exp\left(\frac{j-1}{m-1} \right) - 1}{e - 1} \quad , \quad j = 1, 2, \cdots\cdots, m \quad , \tag{15}$$

with $\delta_o = \delta_m = \pi/2 - \alpha - \theta$, the upper bound of the computational domain of δ. With the definition of Eq. (15), the mid-plane of the wedge is represented by $\delta_1 = 0$. Once δ_j is selected, the grid points in ξ-direction is then determined by the intersection points between the δ_j-ray and the solid wall of the wedge, i.e.,

$$\xi_w(i) = \cos\theta / \sin(\alpha + \delta_{m-i+1}) \quad , \quad i = 1\,, 2\,, \cdots\cdots, m \ . \qquad (16)$$

Equation (16) indicates that $\xi_w(1) = 1$ is the grid point located at the contact line between the liquid and the wedge wall and $\xi_w(m)$ is the grid point at apex of the wedge. By defining $\Delta\xi_k = \xi_w(k+1) - \xi_w(k)$, $\xi_{k+1} = \xi_k + \Delta\xi_k$, with $\xi_1 = \xi_w(1)$, the whole computational grid system is then represented by (ξ_i, δ_j) , with $i, j = 1, 2, \cdots\cdots, m$. Specifically, the grid points on the free surface are denoted by $(\xi_1 \delta_j)$ with $j = 1, 2, \cdots\cdots, m$. The grid systems generated by this scheme for different combinations of the half-wedge angle α and contact angle θ are shown in Fig. 2. It can be seen that the distributions of grids for most of the (α, θ)-combinations are pretty uniform except the one with a zero contact angle wherein the distribution of the grids near the free surface is much closer than elsewhere. Furthermore, because of the nonequally spaced grid distribution, the finite difference scheme has to be modified accordingly to assure a second-order accuracy. Equation (11) is then computed to obtain $v_Z(\xi, \delta)$ followed by the calculations of the averaged velocity $\bar{v}_Z$ and the flow coefficient F_i. Equation (6) is then used to numerically compute $\widetilde{F}$ by a backwards Runge-Kutta method. The variation of the free surface $h(Z, \tilde{t})$ and the tip location $l_{tip}(\tilde{t})$ can then be obtained accordingly.

Before the results are presented and discussed, two important aspects regarding the reliability of the numerical scheme employed need to be clarified. (1). The grid independence has been tested using different grid systems and is shown in Fig. 3. A (40×40) grid system is finally chosen for the reason of accuracy and computational time saving. (2). The flow situation with a zero shear stress on the free surface as considered by Weislogel and Lichter 〔19〕 is recomputed for the purpose of comparison. The results give almost no difference between the computations by Weislogel and Lichter 〔19〕 and the present study.

IV. Results and Discussion

IV-1 Numerical Results

In this subsection, the numerical results of v_Z, $\bar{v}_Z$, F_i, $h(Z,\tilde{t})$, and $l_{tip}(\tilde{t})$ will be systematically presented and discussed. The main concern will be the effects due to the shear stress distribution along the free surface.

When a constant shear stress distribution is imposed on the free surface, Eq. (6) is still valid and similarity solutions exist. However, depending on the magnitudes and directions of the shear stress, the flow structure and, consequently, F_i are different.

(A) S effects on v_Z, $\bar{v}_Z$, and F_i:

The v_Z-distribution at each cross section for $S=-0.075$, 0, and 0.075 with $\alpha=45°$ and $\theta=30°$ are shown in Fig. 4. When S is a negative value, the shear stress is acting in the flow direction and, therefore, the flow is strengthened. When the shear stress is opposing the flow direction, i.e., when S is positive, a reverse flow may exist in the corner region near the free surface. The flow structure becomes completely different. Shown in Fig. 5 are the flow distributions for $S=0.05$, 0.075, and 0.1 with $\alpha=45°$ and $\theta=30°$. It can be seen that when $S=0.05$, the reverse flow starts to occur from the upper corner near the free surface where the inertia of the fluid is smallest due to the no-slip boundary condition at the solid wall. As S increases, the reverse flow region extends toward the central portion of the cross section of the wedge flow and becomes larger and larger. Consequently, the averaged velocity $\bar{v}_Z$ and the flow coefficient F_i at each cross section will change as S varies. Listed in Table 1 are the variations of $\bar{v}_Z$ and F_i with S for $\alpha=45°$ and $\theta=30°$, and the corresponding diagrams are shown in Fig. 6. It can be seen that both $\bar{v}_Z$ and F_i decrease linearly as S increases. It is also indicated in this Table that when $S\approx 0.1$, the region of the reverse flow becomes so large that both $\bar{v}_Z$ and F_i turn to be negative values. Figure 7 gives the variations of F_i with α for different values of θ. Figure 7(a), (b), and (c) are, respectively, the F_i-variation for $S=-0.005$, 0, and 0.0005. Figure 7(b) is the flow situation with a zero-shear boundary condition at the free surface and is the same as that calculated by Weislogel and Lichter 〔19〕. Although the range of F_i is different for different values of S, they all vary similarly. For each half-wedge angle, α, F_i increases as the contact angle θ increases. However, for each contact angle θ, F_i, in general, possesses a minimum value at a certain half-wedge angle α. The shear stresses applied on the free surface possess a much stronger effect on F_i for flow situation with a large half-wedge angle and a small contact angle.

Since F_i is the same constant for all the cross sections with fixed values of α and θ, Eq. (6) and the corresponding similarity solutions are therefore valid for a capillary wedge flow with a constant-shear boundary condition at the free surface.

(B) S effects on h and l_{tip}:

Once F_i is computed, the variations of h and l_{tip} can then be derived from the similarity solutions $\widetilde{F}$ of Eq. (6). Two flow regimes are to be studied. When $a = 0.2$, the solutions correspond to the constant-flow-rate regime while $a = 0$ corresponds to the constant-height regime.

For the convenience of presentation of the numerical results, the extra degree of freedom for the similarity variable, λ, is set equal to unity. Then, the variations of $h(z,t,S)$ with $\alpha = 45°$ and $\theta = 30°$ are plotted in Figs. 8 and 9. Figure 8 is for the constant-flow-rate regime with $S = -0.01$, 0, and 0.001 while Fig. 9 is for the constant-height regime. A lot of information can be learned from those two figures. (1) When the shear stresses act in the flow direction, i.e., when S is a negative value, the wedge flow possesses a larger flow rate and flow speed. (2) As time proceed it seems that the flow possesses a tendency of moving from the constant-flow-rate regime toward the constant-height regime. (3) In both the flow regimes, the flow speed and, consequently, the tip motion slow down as time proceeds.

The tip location of a wedge flow, l_{tip}, in the constant-flow-rate regime and the constant-height regime are shown, respectively, in Figs. 10 and 11. Although l_{tip} is a function of S, the moving speed of the tip location, i.e., dl_{tip}/dt, is independent of S and can be calculated easily and directly from the log-log diagrams in Figs. 10 and 11. The results yield $l_{tip} \propto t^{3/5}$ in the constant-flow-rate regime and $l_{tip} \propto t^{1/2}$ in the constant-height regime, same as derived by Weislogel and Lichter 〔19〕.

IV-2. Scaling Analysis

According to the study by Weislogel and Lichter [19], there may be exist three flow regimes during the motion of a corner flow. These three flow regimes are (1) the start-up transient regime for small t, followed by (2) the constant-flow-rate regime, and then (3) the constant –height regime. A schematic diagram of these three flow regimes is shown in Fig. 12. In the absence of gravity, the corner flow is mainly driven by the capillary pumping force which basically is the pressure difference generated by the free surface curvature at two different locations. This pumping force will be balanced by either the acceleration of the flow during the first transient period or by the viscous shear stresses in the constant-flow-rate and constant-height regimes. In this sub-section, the relation between the tip location of the corner flow and time will be predicted by the scaling analysis of the Z-momentum equation.

(A) Start-up transient regime:

The balance between the acceleration of the flow and the pumping force of the Z-momentum equation can be express as

$$\frac{\Delta P}{L_o} \sim \rho \frac{W_o}{\tilde{t}} , \tag{16}$$

where ΔP represents the characteristic pumping force for the corner flow; L_o, a characteristic length scale in the flow direction whose variation with time gives the motion of tip of the corner flow; $W_o \equiv L_o/\tilde{t}$, the characteristic velocity of the corner flow; ρ and $\tilde{t}$, respectively, the density and time. In the start-up transient period, the pumping force mainly comes from the ambient pressure, P_a, acting on the base liquid in the container. As a result, $\Delta P \sim P_a$ is an appropriate choice for the estimation of the pumping force. Equation (16) then reduces to

$$\frac{P_a}{L_o} \sim \frac{\rho L_o}{\tilde{t}^2} . \tag{17}$$

Since P_a and ρ are constants, Eq. (17) then gives the following relation between the tip location and time

$$L_o \propto \tilde{t} . \tag{18}$$

(B) Constant-flow-rate regime:

In this flow regime, the assumptions given in Section II are applicable. The capillary pumping force is therefore balanced by the viscous shear stresses, which gives

$$\frac{\Delta P}{L_o} \sim \mu \frac{W_o}{H_o^2} \ , \tag{19}$$

with $\Delta P \sim \frac{\sigma}{H_o}$ estimated by the curvature effect of capillarity; $W_o \sim \frac{L_o}{\tilde{t}}$; and the characteristic height $H_o \sim \left(\frac{\dot{\tilde{Q}} \cdot \tilde{t}}{L_o} \right)^{1/2}$ evaluated from the constant flow rate $\dot{\tilde{Q}}$.

Equation (19) then reduces to

$$\frac{\sigma}{L_o} \left(\frac{L_o}{\dot{\tilde{Q}} \cdot \tilde{t}} \right)^{1/2} \sim \frac{\mu \cdot L_o}{\tilde{t}} \left(\frac{L_o}{\dot{\tilde{Q}} \cdot \tilde{t}} \right) \ , \tag{20}$$

which can be re-written as

$$L_o^{5/2} \sim \left(\frac{\dot{\tilde{Q}}^{1/2} \cdot \sigma}{\mu} \right) \cdot \tilde{t}^{3/2} \ . \tag{21}$$

Since $\dot{\tilde{Q}}$, σ, and μ are constants, Eq. (21) then gives the following relation between the tip location and time

$$L_o \propto \tilde{t}^{3/5} \ . \tag{22}$$

(C) Constant-height regime:

Since all the assumptions described in Section II are still valid, Eq. (19) is also applicable in this flow regime. However, the capillary pumping force is estimated by the curvature effect of capillarity with the characteristic height H_o chosen directly equal to the specific constant height H_c of the present situation. Consequently, Eq. (19) reduces to

$$\frac{\sigma}{L_o H_c} \sim \frac{\mu \cdot L_o}{H_c^2 \cdot \tilde{t}} \ , \tag{23}$$

which can be re-written as

$$L_o^2 \sim \left(\frac{\sigma H_c}{\mu} \right) \cdot \tilde{t} \ . \tag{24}$$

Since σ, μ, and H_c are constant, Eq. (24) then gives the following relation between the tip location and time

$$L_o \propto \tilde{t}^{1/2} \ . \tag{25}$$

Equations (18), (22), and (25) are exactly the same as those obtained by Weislogel and Lichter 〔19〕.

V. Conclusions

The system analyzed is the transient capillary wedge flow with a constant shear stress distribution imposed on the free surface. With the assumptions of small inertia, micro-gravity, a slender liquid column with negligible surface curvature along the flow direction, and a constant shear stress distribution on the free surface, the similarity solutions as suggested by Weislogel and Lichter 〔19〕 are still valid. The following conclusions are drawn from the present study. (1) When the shear stresses act in the flow direction, the flow is strengthened and, as a result, the propagation of the tip location becomes faster while as the shear stresses are opposing the flow direction, a reverse flow may exist in the corner region near the free surface. The reverse flow region extends toward the central portion of the cross section of the wedge flow when the countercurrent shear stresses become stronger. (2) As time proceeds, the wedge flow possesses a tendency to move from the constant-flow-rate regime toward the constant-height regime. (3) In both the flow regimes, the flow speed and, consequently, the motion of the tip location slow down as time proceeds.

When the half-wedge angle, the contact angle, and the shear stress distribution on the free surface vary along the flow direction, the similarity solutions as suggested by Weislogel and Lichter 〔19〕 may not exist. Numerical computations then become necessary. When the velocity component normal to the contact line is significant, the static (constant) contact angle assumption becomes invalid. As a result, the dynamic contact angle effects need to be considered.

Reference:

1. Columbus, R. L. and Palmer, H. J., 1987, Architectured Fluid Management of Biological Liquids. *Clinical Chemistry*, Vol. 33 (9), pp. 1531-1537.
2. Jaekle, D. E. JR, 1991, Propellant Management Device Conceptual Design and Analysis: Vanes. *AIAA* Paper, pp. 91-2172.
3. Rollins, J. R., Grove, R. K. and Jaekle, D. E. JR, 1985, Twenty three years of Surface Tension Propellant Management System Design, Development, Manufacture, Test, and Operation. *AIAA* Paper, pp. 85-1199.
4. Concus, P. and Finn, R., 1969, On the Behavior of a Capillary Surface in a Wedge. *Appl. Math. Sci.*, Vol. 63, pp. 229-299.
5. Concus, P. and Finn, R., 1974, On Capillary Free Surfaces in the Absence of Gravity. *Acta. Math.*, Vol. 132, pp. 177-198.
6. Concus, P. and Finn, R., 1974, On Capillary Free Surfaces in a Gravitational Field. *Acta. Math.*, Vol. 132, pp. 207-223.
7. Concus, P. and Finn, R., 1990, In Low-Gravity Fluid Dynamics and Transport Phenomena. (ed. Koster, J. N. and Sani, R. L.). *Progress in Astronautics and Aeronautics*, Vol. 130, pp. 183-204. AIAA.
8. Lazzer, A. DE., Langbein, D., Dreyer, M. and Rath, J., 1996, Mean Curvature of Liquid Surfaces in Containers of Arbitrary Cross-Section. *Microgravity Sci. Technol.*, IX(3), pp. 208-219.
9. Mason, G. and Morrow, N., 1991, Capillary Behavior of a Perfectly Wetting Liquid in Irregular Triangular Tubes. *J. Colloid Interface Sci.*, Vol. 141, pp. 262-274.
10. Ayyaswamy, P. S., Catton, I., and Edwards, D. K., 1974, Capillary Flow in Triangular Grooves. *Trans. ASME: J. Appl. Mech.*, Vol. 41, pp. 332-336.
11. Dong, M. and Chatzis, I., 1995, The Imbibition and Flow of a Wetting Liquid along the Corners of a Square Capillary Tube. *J. Colloid Interface Sci.*, Vol. 172, pp. 278-288.
12. Kolb, W. B. and Cerro, R. L., 1993, The Motion of Long Bubbles in Tubes of Square Cross Section. *Phys. Fluids A.*, Vol. 5, pp. 1549-1557.
13. Legait, B., 1983, Laminar Flow of Two Phases through a Capillary tube with Variable Square Cross-Section. *J. Colloid Interface Sci.*, Vol. 96, pp. 28-38.
14. Ma, H. B., Peterson, G. P., and Lu, X., 1994, The Influence of Vapor-Liquid Interactions on the Liquid Pressure Drop in Triangular Microgrooves. *Intl J. Heat Mass Transfer.*, Vol. 37, pp. 2211-2219.
15. Peterson, G. P. and Ma, H. B., 1996, Analysis of Countercurrent Liquid-Vapor

Interactions and the Effect on the Liquid Friction Factor. *Exp. Thermal Fluid Sci.*, Vol. 12, pp. 13-24.

16. Ransohoff, T. C. and Radke, C. J., 1988, Laminar Flow of a Wetting Liquid along Corners of a Predominantly Gas-Occupied Noncircular Pore. *J. Colloid Interface Sci.*, Vol.121, pp. 392-401.
17. Weislogel, M. M., 1996, Capillary Flow in an Interior Corner. PhD Thesis, Northwestern Univ.
18. Weislogel, M. M. and Lichter, S., 1996, A Spreading Drop in an Interior Corner: Theory and Experiment. *Microgravity Sci. Technol.*, IX (3), pp. 175-184.
19. Weislogel, M. M. and Lichter, S., 1998, Capillary Flow in an Interior Corner. *J. Fluid Mech.*, Vol. 373, pp. 349-378.
20. Lagbein, D., 1990, The Shape and Stability of Liquid Menisci at Solid Edges. *J. Fluid Mech.*, Vol. 213, pp. 251-265.
21. Hu, H. H. and Joseph, D. D., 1989, Lubricated Pipelining: Stability of Core-Annular Flow. Part 2. *J. Fluid Mech.*, Vol. 205, pp. 359-396.
22. Dussan, V., E. B., 1979, On the Spreading of Liquids on Solid Surface Static and Analysis: Vanes. *AIAA* Paper, pp. 91-2172.
23. Hoffman, R. L., 1995, A Study of the Advancing Interface: I. Interface Shape in Liquid-Gas Systems. *J. Col. Inter. Sci.*, Vol. 50, p. 228.
24. Weislogel, M. M., 1997, Spontaneous Steady Capillary Flow in Partially Coated Tubes. *AIChE J.*, Vol. 43, pp. 645-654.

Nomenclature

A	nondimensionalized cross-sectional area by H_0^2
Bo	Bond number
F	similarity solution
F_A	shape factor; $F_A \equiv A/h^2$
F_i	flow coefficient
$\widetilde{F}$	modified similarity solution; $F = \lambda^2 \widetilde{F}$
f	defined as $\left(\sigma H_0 \sin^2 \alpha \big/ \mu L_0 \right) \big/ W_0$
g	gravitational acceleration
H	dimensional height of the free surface at $x = 0$
H_c	the specific constant height in constant-height flow regime
H_0	reference length scale in Y - direction
h	nondimensionalized H by H_o
L_o	reference length scale in Z - direction
L_{tip}	tip location of the corner flow
l_{tip}	nondimensionalized L_{tip} by L_o
P	dimensional pressure
P_a	ambient pressure
$\dot{Q}$	volume flow rate; dimensionless
$\dot{\widetilde{Q}}$	volume flow rate; dimensional
r	radial coordinate; dimensional
r_c	radius of the circular arc of the free surface
S	shear stress distribution along the free surface; dimensionless
t	nondimensionalized time by L_o/W_o
$\widetilde{t}$	time; dimensional
v_Z	nondimensionalized Z -velocity by $\left[r_c^2 \cdot (-dP/dZ)/\mu \right]$
$\bar{v}_z$	averaged v_z -velocity
W	velocity in Z -direction; dimensional
W_o	a reference Z - velocity defined as L_o/t

w	nondimensionalized Z-velocity by $\left(\sigma \cdot H_o \cdot \sin^2 \alpha \big/ \mu \cdot L_o\right)$
$\overline{w}$	averaged w-velocity
X	coordinate in X-direction; dimensional
x	dimensionless X-coordinate; $x = X \big/ H_o \tan\alpha$
Y	coordinate in Y-direction; dimensional
y	dimensionless Y-coordinate; $y = Y/H_o$
Z	coordinate in Z-direction; dimensional
z	dimensionless Z-coordinate; $z = Z/L_o$

α	half-wedge angle
δ	azimuthal angle
δ_0	upper bound of δ-angle
η	similarity variable
$\tilde{\eta}$	modified similarity variable; $\eta = \lambda\tilde{\eta}$
μ	dynamic viscosity
ρ	density
σ	surface tension
Σ	location of the free surface
τ	defined as $F_i \cdot t/2$
θ	contact angle

Table 1. Variations of $\bar{v}_z$ and F_i with S for $\alpha = 45°$ and $\theta = 30°$.

S	$\bar{v}_z$	F_i
-0.2	1.07E-02	0.4219
-0.15	8.85E-03	0.3505
-0.1	7.05E-03	0.2791
-0.05	5.25E-03	0.2077
-0.01	3.80E-03	0.1506
-0.005	3.62E-03	0.1435
-0.001	3.48E-03	0.1378
-0.0005	3.46E-03	0.137
0	3.44E-03	0.1363
0.0005	3.43E-03	0.1356
0.001	3.41E-03	0.1349
0.005	3.26E-03	0.1292
0.01	3.08E-03	0.1221
0.05	1.64E-03	0.0649
0.1	-1.63E-04	-0.00644
0.15	-1.97E-03	-0.0778
0.2	-3.77E-03	-0.1492

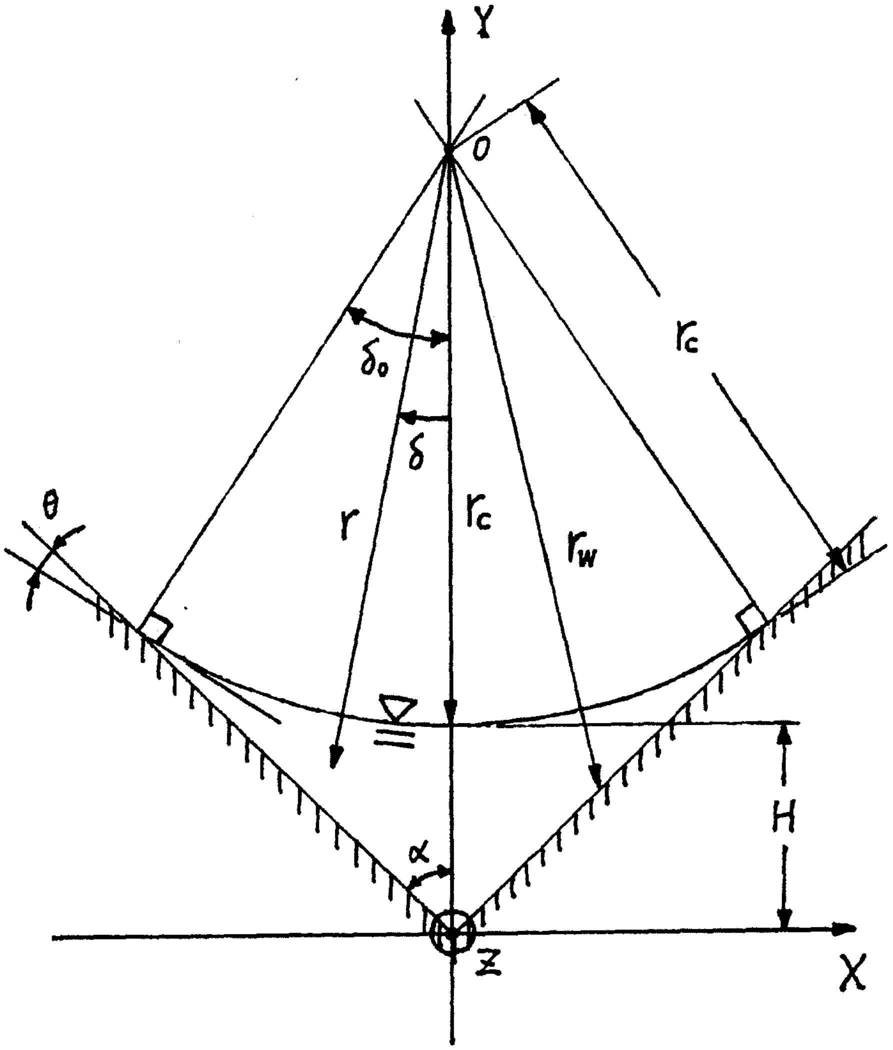

Figure 1. The schematic diagram of the physical model and the coordinate system.

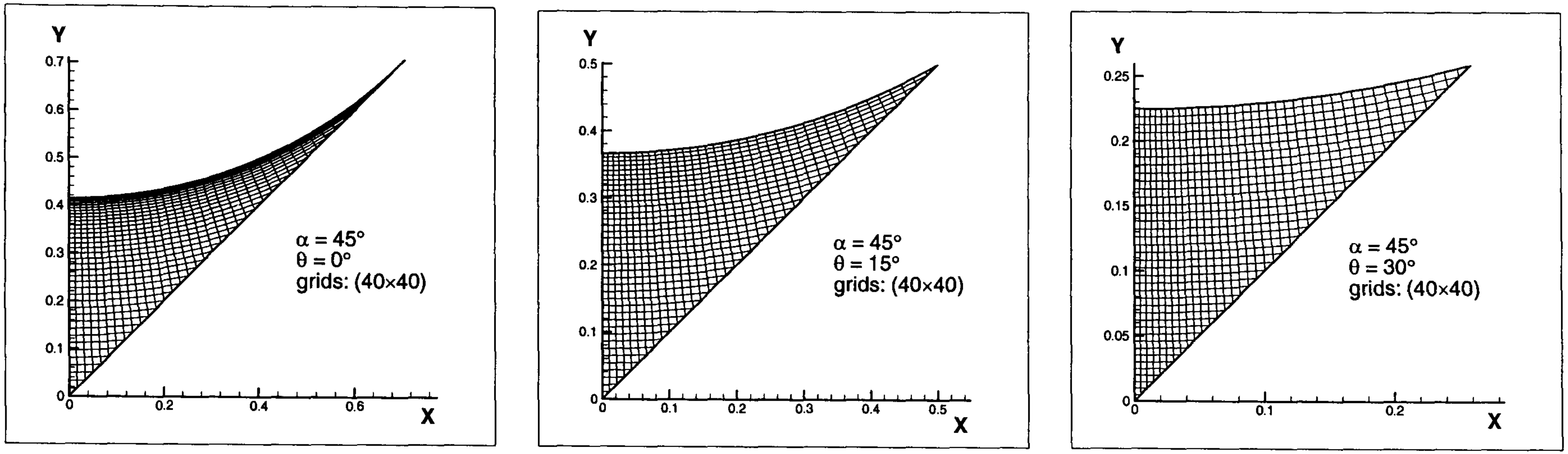

Figure 2. The computational grid systems for various combinations of α and θ.

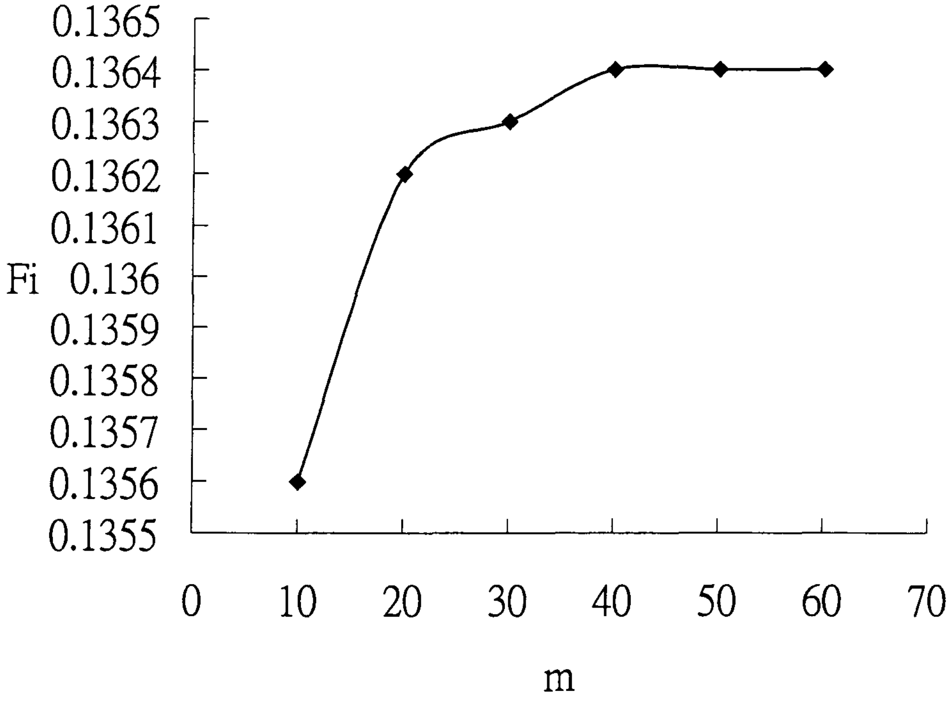

Figure 3. Comparison of F_i computed with different grid systems for $\alpha = 45°$ and $\theta = 30°$.

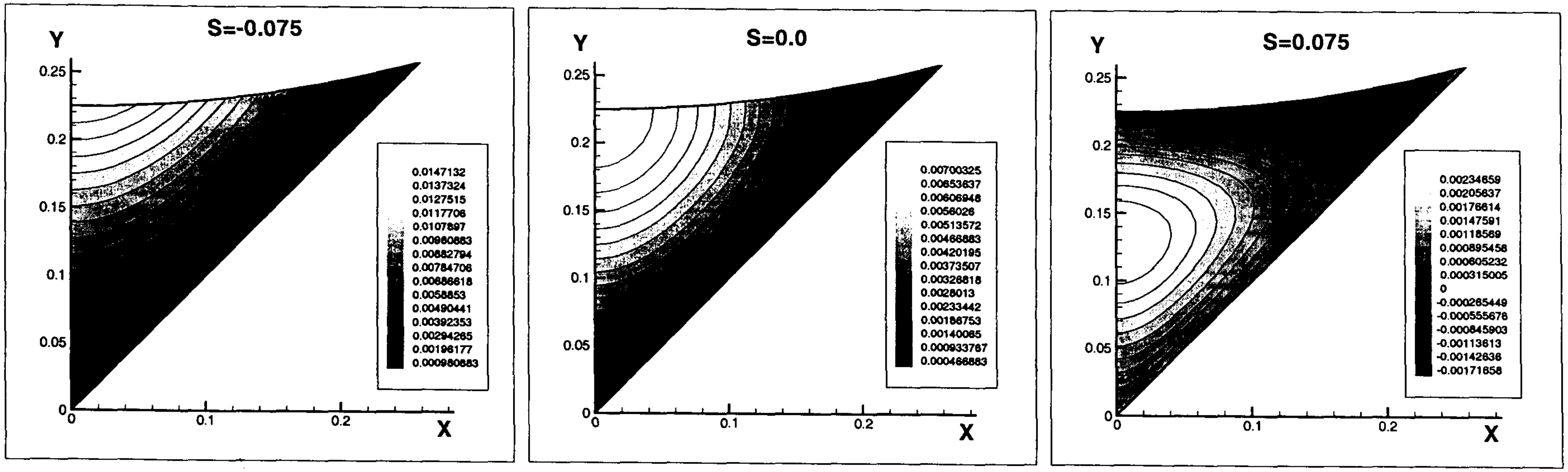

Figure 4. v_z-distribution for $S = -0.075$, 0.0, and 0.075 with $\alpha = 45°$ and $\theta = 30°$.

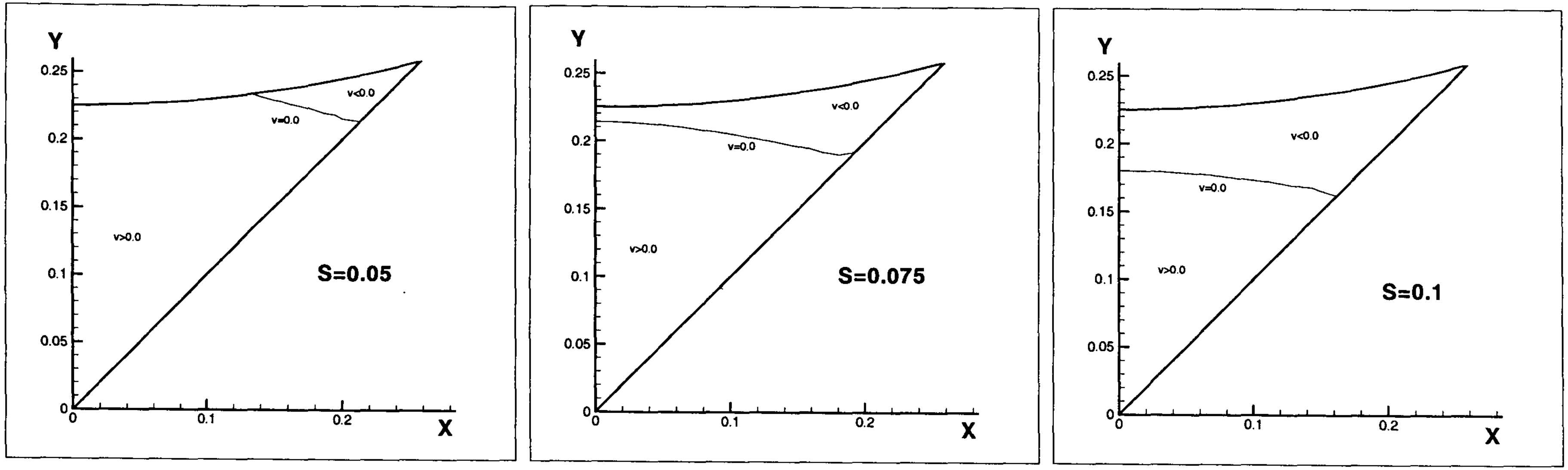

Figure 5. v_z-distribution for $S = 0.05$, 0.075, and 0.1 with $\alpha = 45°$ and $\theta = 30°$.

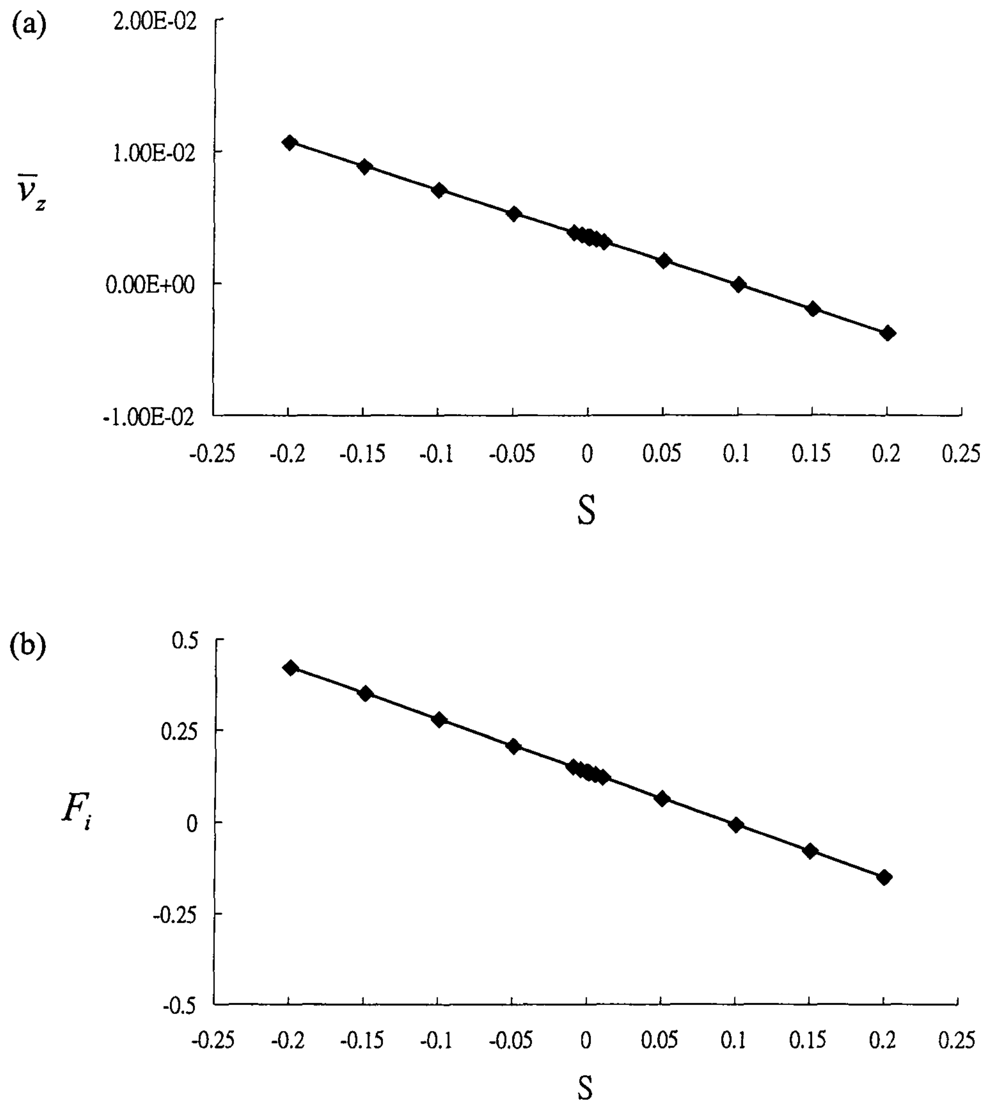

Figure 6. Variations of $\bar{v}_z$ and F_i with S for $\alpha = 45°$ and $\theta = 30°$; (a) $\bar{v}_z$ vs. S, and (b) F_i vs. S.

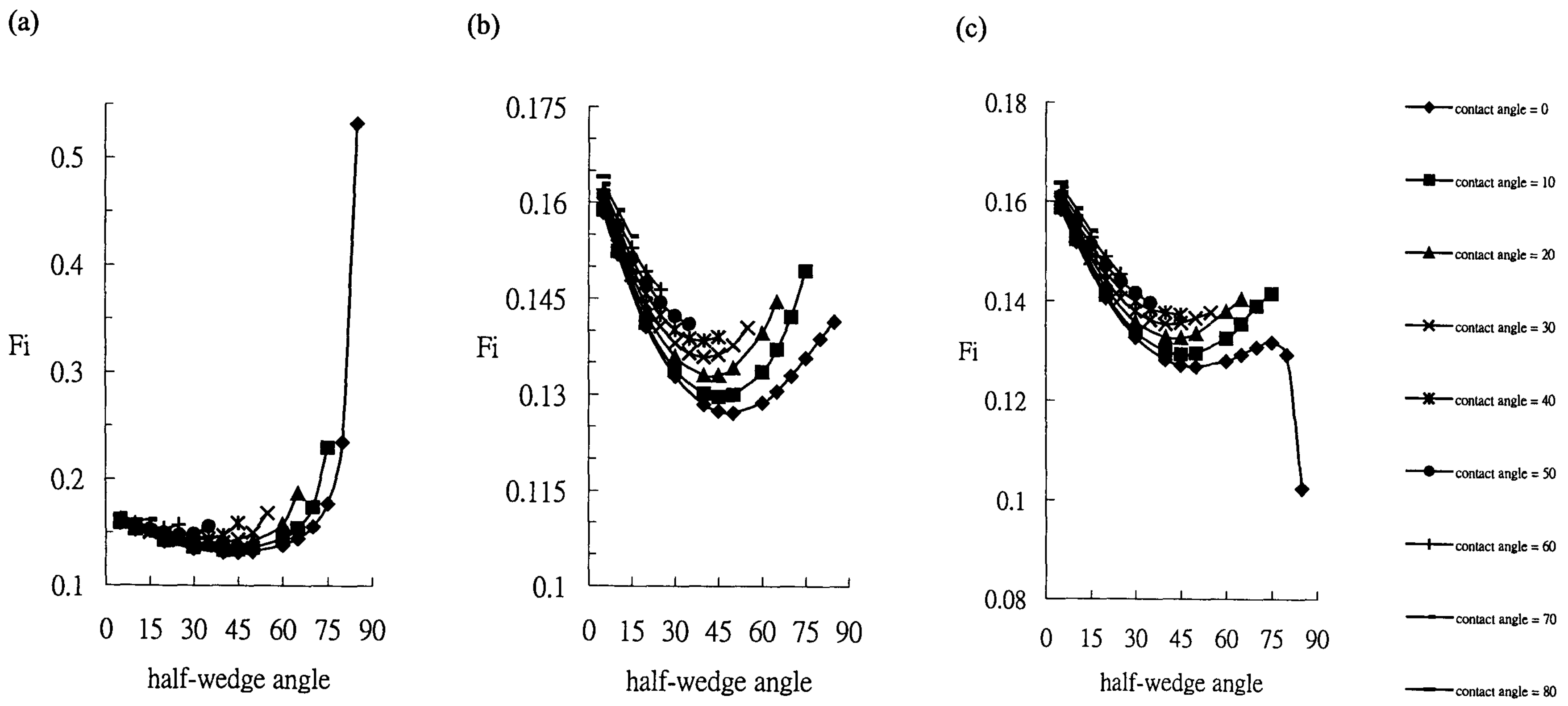

Figure 7. Variations of F_i and α for different values of θ; (a) $S=-0.005$, (b) $S=0$, and (c) $S=0.0005$.

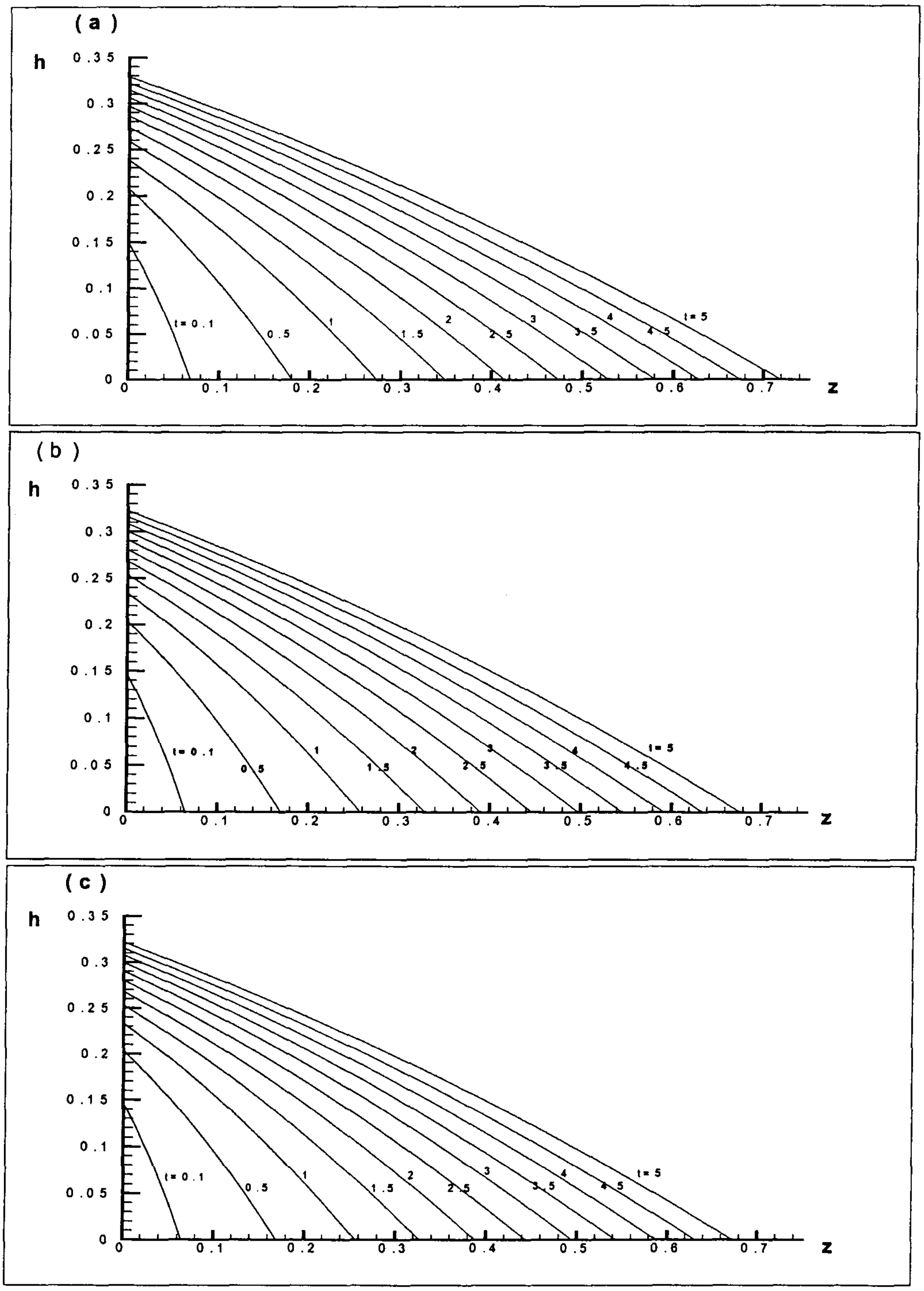

Figure 8. Variations of $h(z,t;S)$ for the constant-flow-rate regime with $\alpha = 45°$ and $\theta = 30°$; (a) $S = -0.01$, (b) $S = 0$, and (c) $S = 0.001$.

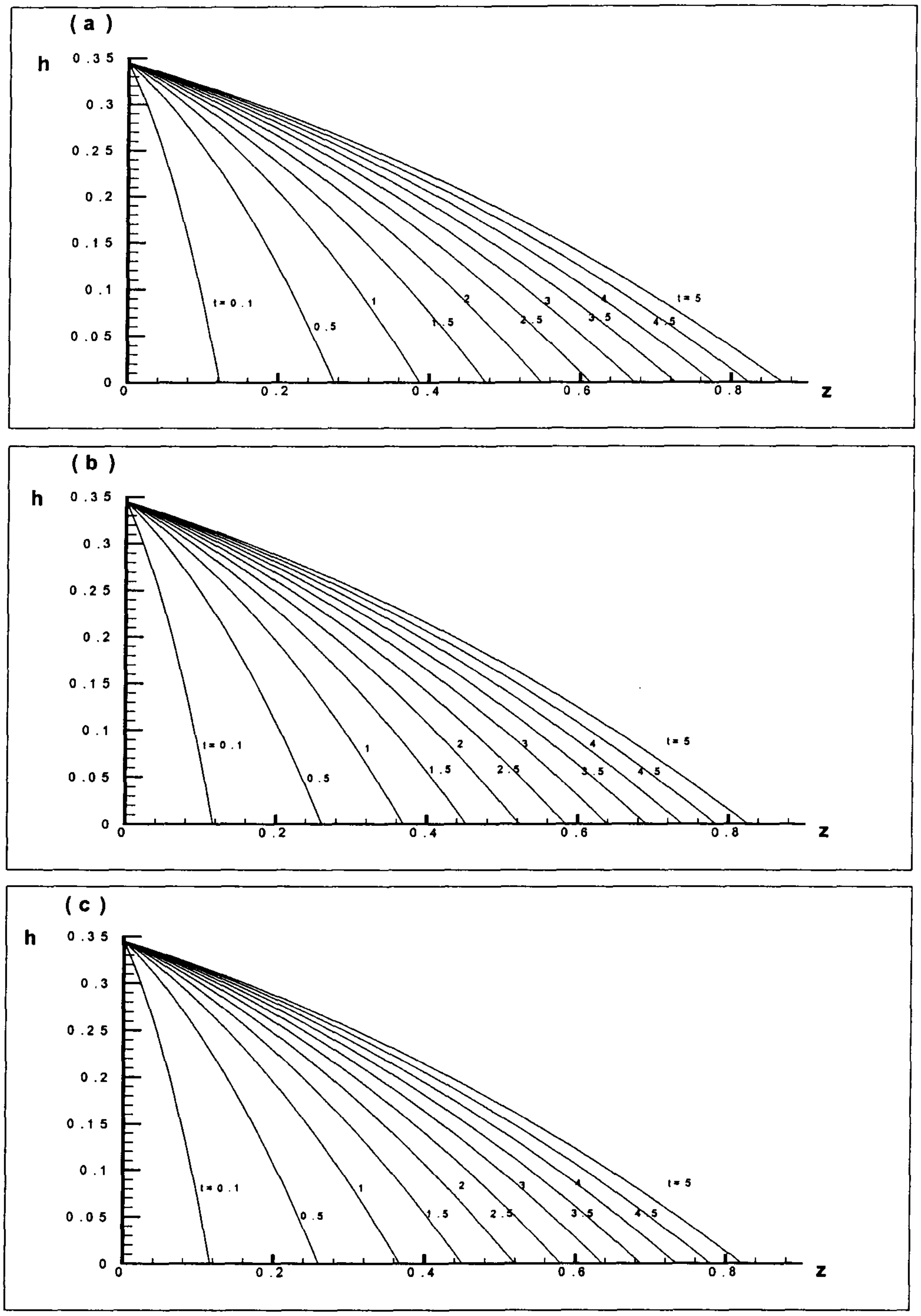

Figure 9. Variations of $h(z,t;S)$ for the constant-height regime with $\alpha = 45°$ and $\theta = 30°$; (a) $S = -0.01$, (b) $S = 0$, and (c) $S = 0.001$.

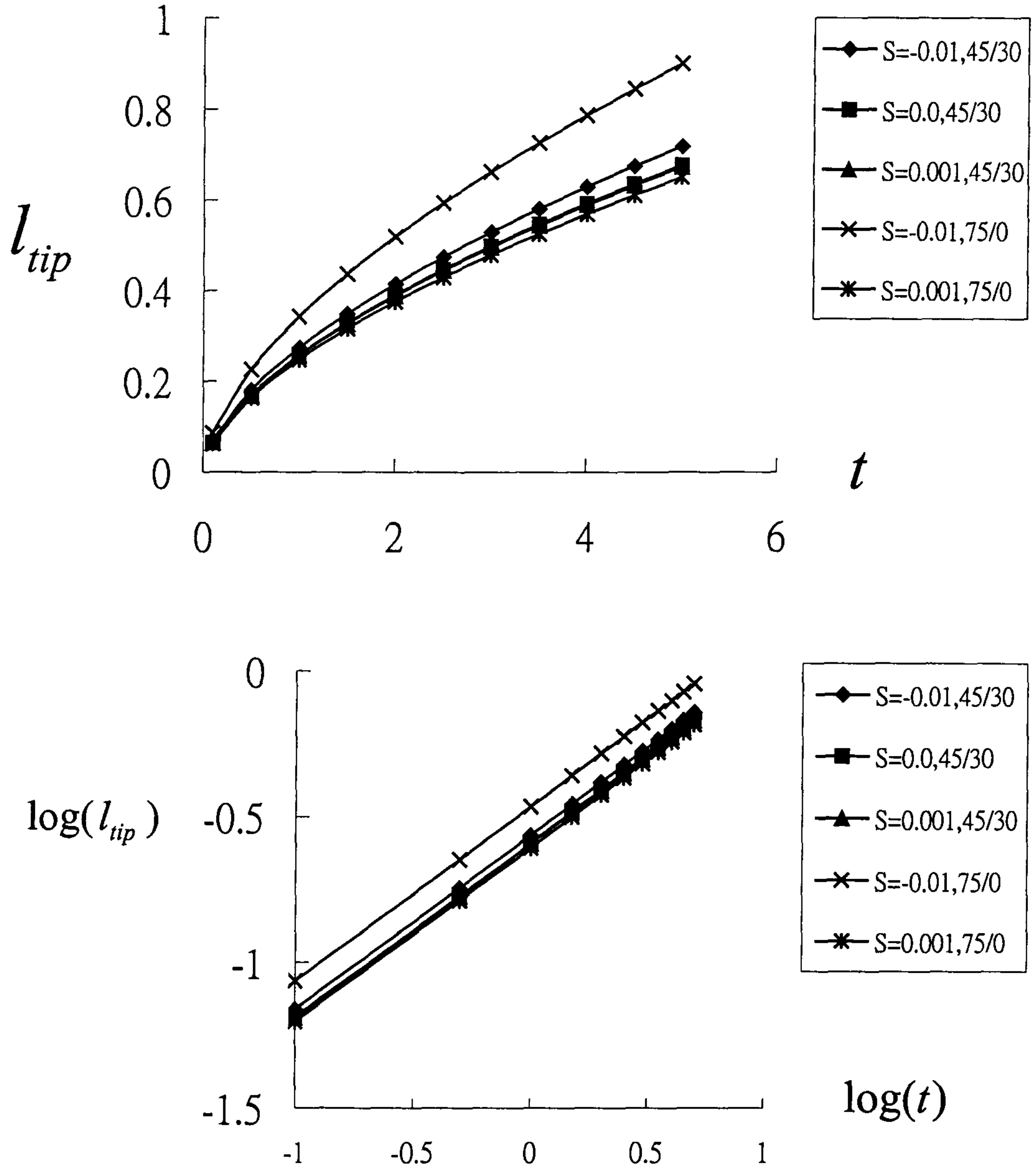

Figure 10. Tip location of a wedge flow in the constant-flow-rate regime.

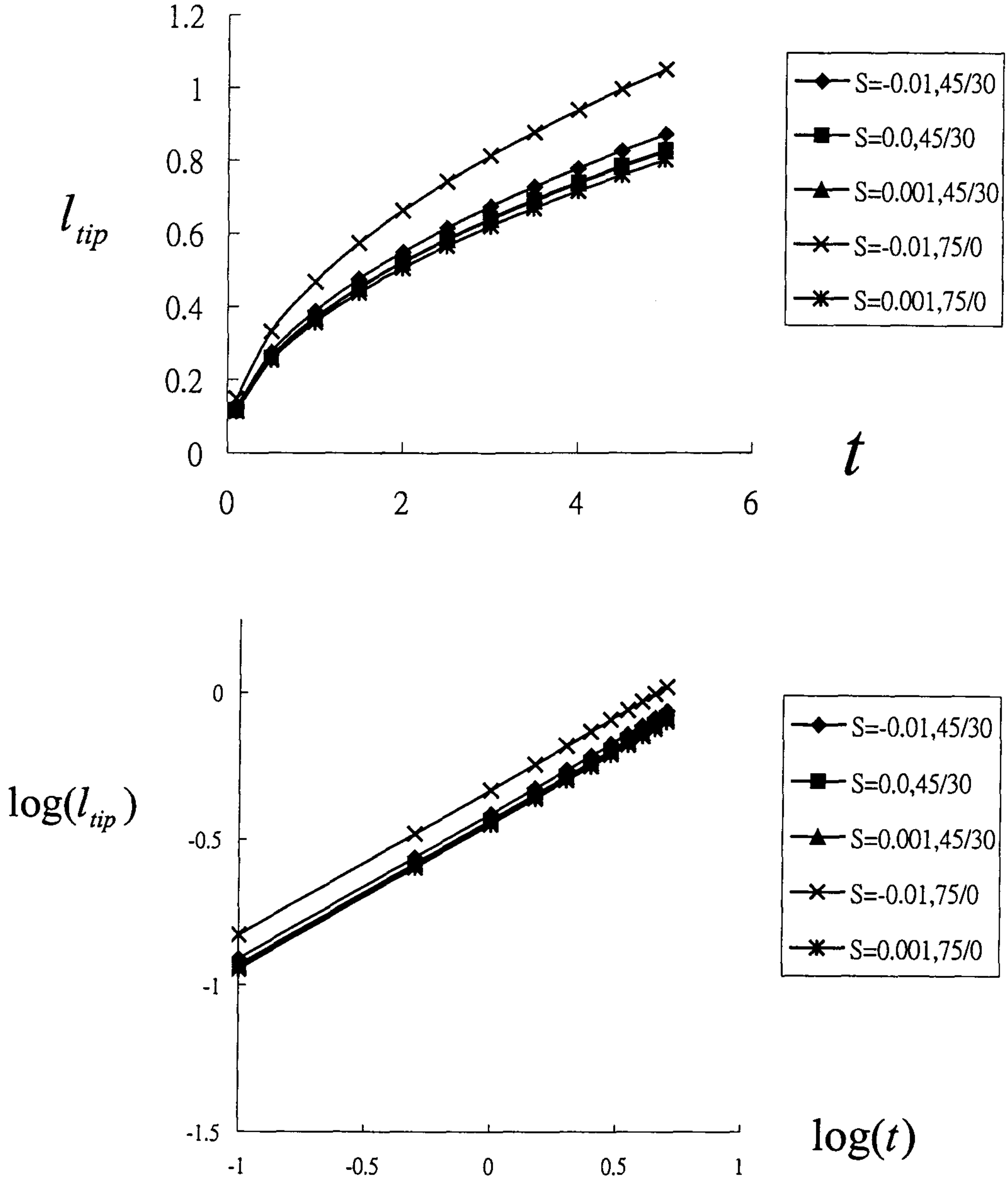

Figure 11. Tip location of a wedge flow in the constant-height regime.

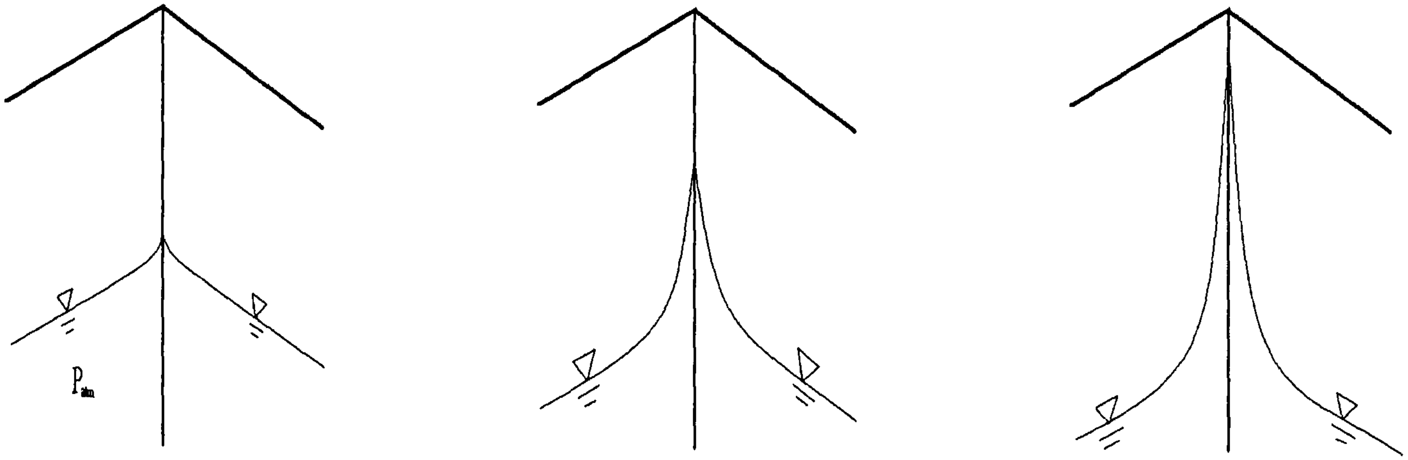

(a) start-up transient regime.

(b) constant-flow-rate regime.

(c) constant-height regime.

Figure 12. Different flow regimes for a capillary corner flow.